

Supporting Information for: A Step in Carbon Capture from Wet Gases: Understanding Water Effect on CO₂ Adsorption and Diffusion in UiO-66

Yann Magnin,^{*,†} Estelle Dirand,[‡] Alejandro Orsikowsky,[¶] Mélanie Plainchault,[§]
Véronique Pugnet,^{||} Philippe Cordier,[‡] and Philip L. Llewellyn^{||}

[†]*Consultant, TotalEnergies@Saclay NanoInnov, 2 boulevard Thomas Gobert, 91120 Palaiseau Cedex, France. On the behalf of TotalEnergies S.E.*

[‡]*TotalEnergies@Saclay NanoInnov, 2 boulevard Thomas Gobert, 91120 Palaiseau Cedex, France.*

[¶]*TotalEnergies, OneTech, Sustainability R&D, PERL, 64170 Lacq, France.*

[§]*TotalEnergies, OneTech, Upstream R&D, CSTJF - Avenue Larribau, 64018 Pau Cedex, France.*

^{||}*TotalEnergies, OneTech, Sustainability R&D, CSTJF - Avenue Larribau, 64018 Pau Cedex, France.*

E-mail: yann.magnin@external.totalenergies.com

UiO-66(Zr) metal-organic framework structure

The UiO-66(Zr) structure¹ is made of zirconium oxide nodes, bridged by terephthalic acid ligands. The resulting nanoporous structure is formed of tetrahedral and octahedral cages with diameters of ~ 0.75 nm and ~ 1.1 nm respectively, linked by a ~ 0.6 nm aperture,² Fig S1. The total pore volume of the structure is around ~ 0.77 cm³/g, with a surface area of

about $\sim 1160 \text{ m}^2/\text{g}$,^{3,4} making it a fully nanoporous MOF, with pore diameters smaller than 2 nm.⁵ Despite its relatively high porosity and pore surface, UiO-66(Zr) has received particular attention due to its well controlled and highly reproducible lab-scale synthesis,⁶ coupled with its high bulk modulus $\sim 40 \text{ GPa}$,⁷ and high thermal, acidic, and water vapor stability, making it a good candidate for industrial applications.^{8,9} The stability of the UiO-66 can be rationalized by strong Zr-O bonds, found to be higher than the C-C ligand bond strengths.¹ Zr-O nodes correspond to low energy sites favoring water adsorption,¹⁰ in addition such a MOF presents a low metal lability with water (*i.e.* large energy gap between frontier orbitals of metal and H_2O), ensuring limited hydrolysis properties, or high water stability.^{11,12} Such properties and the large experimental and theoretical literature available on UiO-66(Zr), made it an ideal model structure to gain insight into CO_2 adsorption and diffusion as a function of the water content.

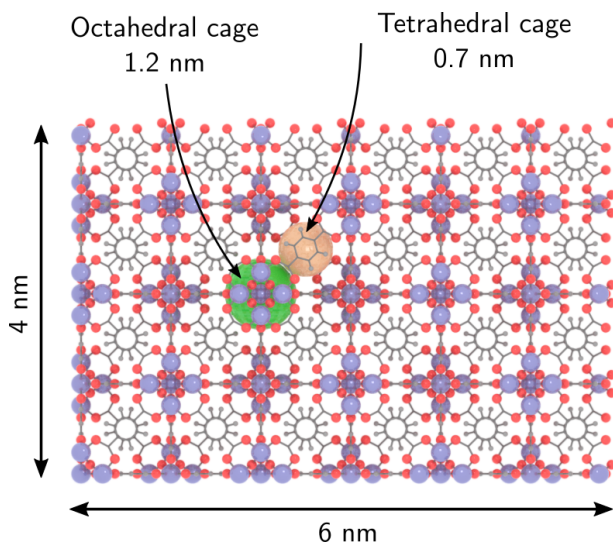


Figure S1: UiO-66 crystal, tetrahedral and octahedral cages are shown by flush and green spheres, respectively. Zirconium, oxygen and hydrogen atoms correspond to purple, red and grey balls.

Adsorbate-adsorbent interactions and host deformation

Simulations performed in flexible MOF structures allow to show a small host contraction as a function of guest loading Fig S2. For CO₂ adsorption, the contraction is found to be smaller than 0.25%, and about 1.5% for H₂O. The slight difference observed is found to depend on the nature of the adsorbates occupying the MOF porosity. For loadings up to ~3 wt%, water molecules form chains into the octahedral cages, pulling nodes closer due to relatively strong H bonds corresponding to the MOF contraction. The effect is however much more moderate for CO₂ with lower guest-guest interactions. While contraction is weak for UiO-66 structure, it has been shown to drive structure collapse in some flexible structures.¹³ Note that UiO-67(Zr), characterized by linkers with one more aromatic cycle (compared to UiO-66), and known as a mesoporous water stable structure (pores larger than 2 nm⁵), remains unstable during the dehydration phase, because of capillary forces, strong enough to induce a compression driving the structure to collapse,¹⁴ and making such a cousin UiO inappropriate for CO₂ capture applications in humid steams.

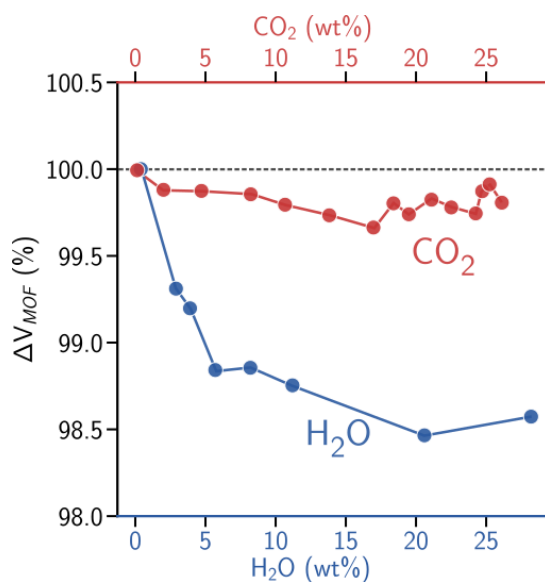


Figure S2: Normalized contraction of the UiO-66(Zr) structure induced by guest molecules CO₂ (red circles) and H₂O (blue circles), as a function of guests loading.

Simulation details

All simulations have been made in a UiO-66 structure of $6 \times 4 \times 4 \text{ nm}^3$, Fig S1. For adsorption simulations we have used the OMC algorithm, in which the MOF structure randomly exchanges molecules with an ideal gas reservoir at a constant guest chemical potential μ , volume V and temperature T , corresponding to a standard grand canonical Monte Carlo simulation (GCMC). A cycle consists in trying 1000 molecule insertions or deletions, randomly chosen with 50% probability. The resulting fluid density thus depends on the thermodynamic parameters (μ, V, T) . Volume equilibration is ensured by 1000 molecular dynamic (MD) steps spanning 1 ps in (N, P, T) ensemble, after each Monte Carlo cycle.

OMC simulations were run for 3×10^7 cycles, for both CO_2 and H_2O isotherms. The first 2×10^7 cycles were used to equilibrate the system and remaining cycles were used for averaging guests density from equilibrium microstates. It is important to note that GCMC simulations do not directly control the pressure, but the chemical potential,

$$\mu = k_B T \ln \left(\frac{f \Lambda^3}{k_B T} \right), \quad (1)$$

with Λ the de Broglie thermal wave length, and f the fugacity. The pressure is determined from f , whose form in Eq.1 depends on the equation of state. In order to get accurate pressures, that deviate from ideal gas under some thermodynamic conditions, fugacity has been corrected from the Soave-Redlich-Kwong (SRK) model.¹⁵

In this work, we have tested different charges models obtain from DFT calculations DDEC,¹⁶ REPEAT,¹⁷ and from the empirical QeQ approach,¹⁸ table S1. Lennard Jones parameters are given in the table S2, and inter-atomic parameters has been calculated from the Lorentz Berthelot mixing rule.

Table S1: MOF partial charges.

Atoms	Zr	O _(O-C)	O _(O-Zr)	C _(C-O)	C _(C-C)	C _(C-H)	H _(H-C)
DDEC	2.573	-0.6761	-1.237	0.747	-0.104	-0.706	0.118
REPEAT	2.449	-0.6983	-0.7187	0.7623	0.0443	-0.1599	0.146
QeQ	1.003	-0.4631	-0.4414	0.5767	-0.0482	-0.0753	0.152

Table S2: Lennard-Jones parameters for adsorbent and adsorbates.

Atoms	Zr	O	C	H	C _{CO₂}	O _{CO₂}	O _{H₂O}	H _{H₂O}
σ (nm)	0.278	0.3118	0.3431	0.2571	0.28	0.305	0.3164	0
ϵ (kcal/mol)	0.069	0.06	0.105	0.044	0.0536	0.157	0.1627	0
q	-	-	-	-	0.7	-0.35	-1.0484	0.5242

MD simulations used to determine diffusion coefficients from the mean square displacement were performed in the (N,P,T) ensemble for 5 ns (pure water) and 10 ns (for multi-component CO₂-H₂O), with a time step of 1 fs. Thermostat and barostat were used in order to keep constant pressure and temperature during full simulations. The binding energy presented in the article has also been determined from MD simulations in the (N,P,T) ensemble. Structure annealing has been run for 10 ns, with a thermal ramp ranging from $T=300\text{K}$ to 5K , with a time step of 1 fs. Binding energies were then determined from instantaneous energy calculations in annealed structures, and have been reproduced 10 times to gain a better average in E_b . Water binding energies have been determined in the same manner (removing the MOF structure after being annealed), by randomly removing one molecule from the water cluster network. Random removing has been made 100 of times to gain a robust statistics.

Charge models effects

Average water energies determined at $T=5\text{K}$ with DDEC and QeQ models are shown in Fig S3A, both showing a decreasing behavior. We note that QeQ (yellow circles) agree well with DFT calculations made by Wang *et al.*¹⁹ (white star). However, a change in behavior is observed at $T=300\text{K}$ where DDEC (red circles) increasing, indicating an hydrophilic behavior at low water loading contrary to QeQ that decreasing, Fig S3B. We then compare adsorption cages favored at low pressure, depending on the two charge models. As can be seen in Fig S4A,B, DDEC predicts water adsorption in tetrahedral cages, in agreement with DFT calculations,^{19,20} while QeQ shows water adsorption in octahedral cages, in line with the results of Calero *et al.*²¹

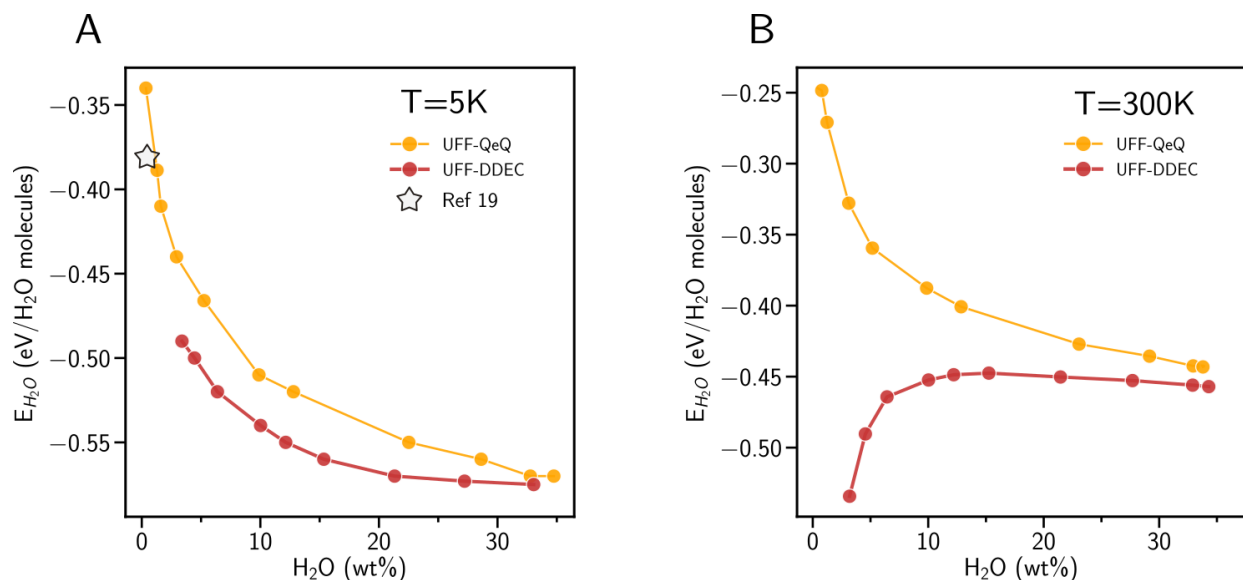


Figure S3: Per-water average energies as a function of the loading. The yellow and red circles correspond to numerical simulations with QeQ and DDEC point charges, respectively. In figure (A), calculations has been made at $T = 5\text{K}$, in figure (B), the same calculation was performed at $T = 300\text{K}$.

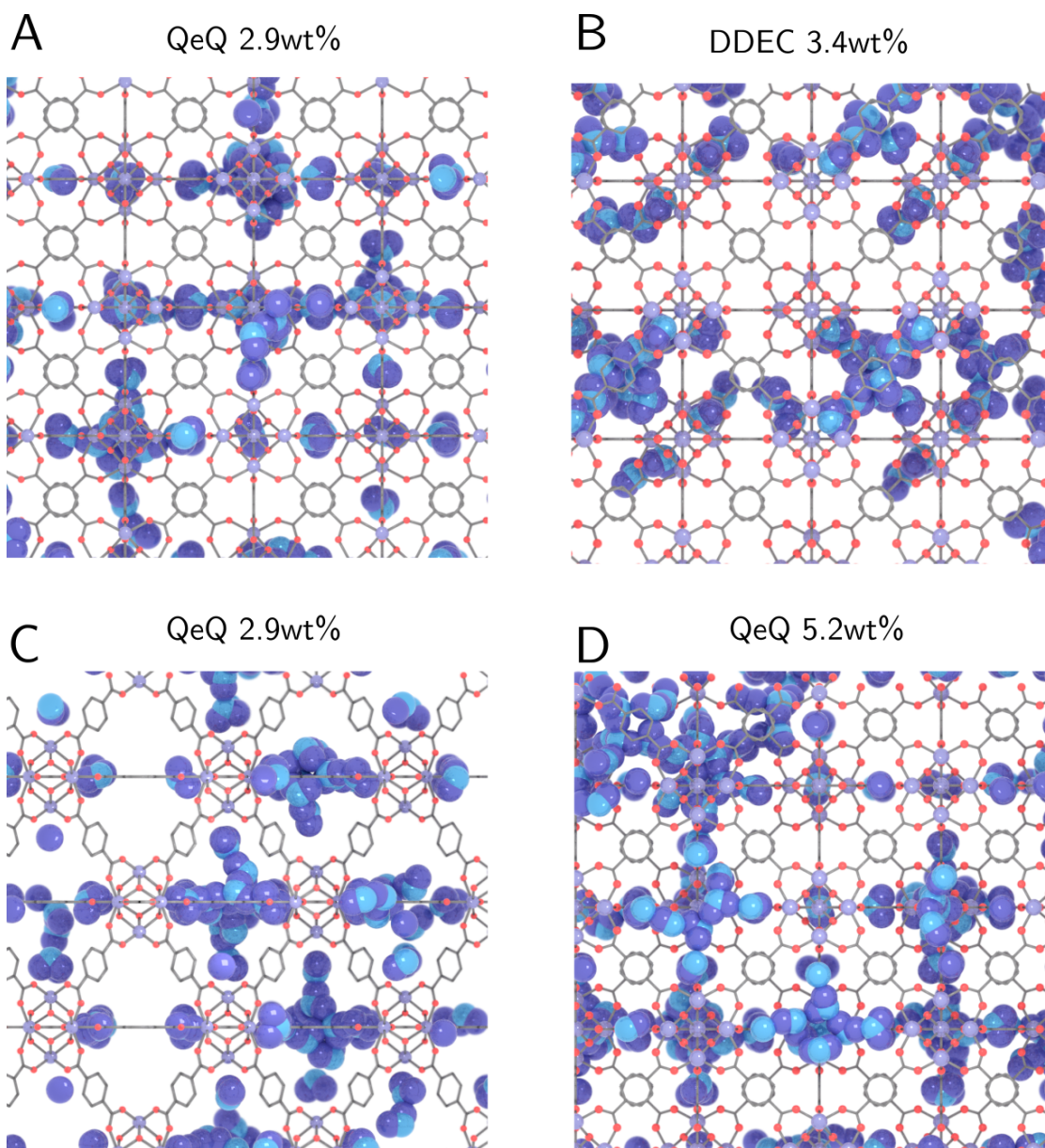


Figure S4: A. Water adsorption favored in octahedral cages using QeQ charge model at $T = 300\text{K}$ for a loading of 2.9 wt%. B. Water adsorption favored in tetrahedral cages using DDEC charge model at $T = 300\text{K}$ for a loading of 3.4wt%. C. Same than (A) under a different view angle. D. Same than (A) with a water loading of 5.2wt%. For a sake of clarity these snapshots are presented in a rigid structure.

Experimental details

Water vapor isotherms presented in the article, were performed by means of an IGAsorp Dynamic Vapour Sorption Analyzer from Hidden Isochema using 35 mg of sample and over a total flow of 500 ml/min (water diluted in helium). The system is fully automated, and can operate from 0% relative humidity (RH), up to 90% RH within a temperature range of 278K to 358K. The adsorption equilibrium tolerance for each relative humidity step is based on the variation of the sample mass, and was set to $\pm 0.002\text{wt}/\text{min}$ within a time limit of 480 min. MOF samples were pretreated *in situ* at a temperature of 423K overnight using integrated electrical heating system under a 500 ml/min helium flow at 1 bar.

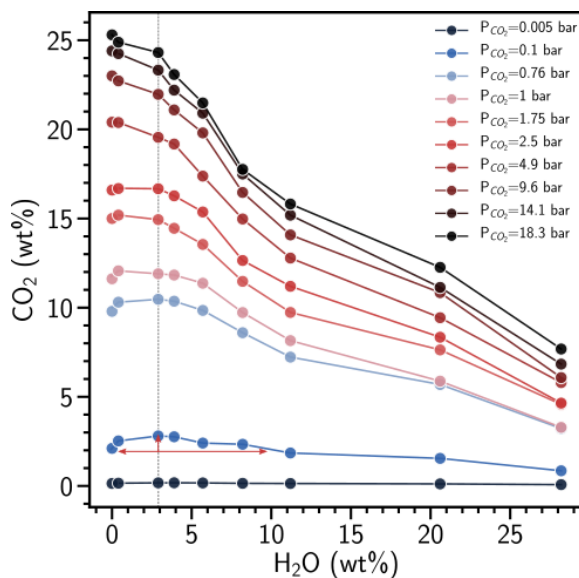


Figure S5: CO_2 concentration as a function of the water loadings pre-adsorbed into the MOF for different CO_2 pressures (legend) by simulations.

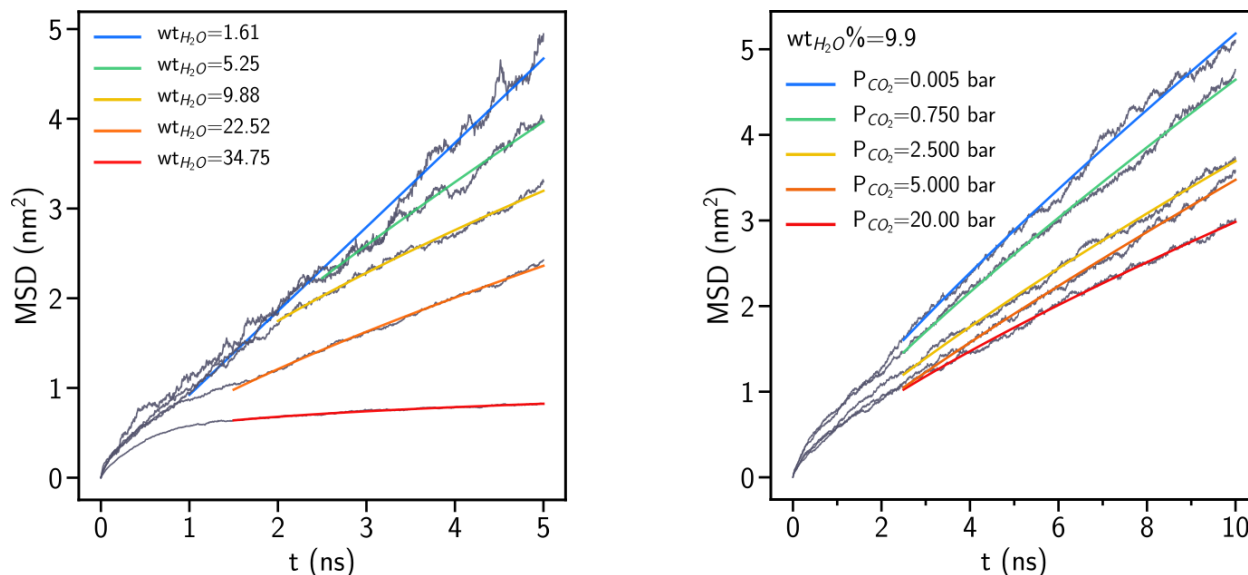


Figure S6: (left panel) Mean square displacement as a function of time for water at different loadings (legend). (right panel) Mean square displacement as a function of time for CO₂ at a water loadings of 9.9 wt% (legend). In the two figures, grey plots correspond to MSD by molecular dynamics, colored plots correspond to fits.

Cluster identification and size distribution

Cluster identification has been evaluated from $O - H$ distances < 0.25 nm on the basis of the maximum H bonds length in the first pic of the water RDF, Fig S8A,B. By screening the overall water molecules adsorbed into the MOF, we generate an adjacency matrix M , in which rows and columns represent water molecules indexes. $M(i, j)$ is thus filled by 1 if molecules $i \neq j$ satisfy the above condition. We then determine from M the connected components following the methodology described in^{22,23} allowing the determination of connected components for all molecules belonging to a cluster.

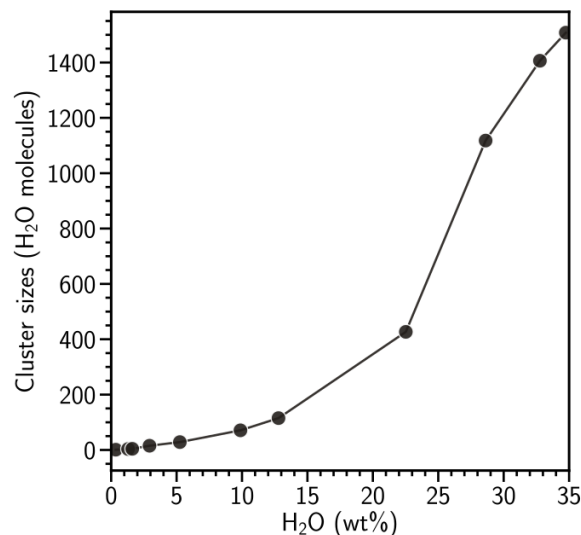


Figure S7: Water cluster sizes distribution for different water concentrations.

Discrete to continuous 3D structure representation

3D water continuum snapshots were performed by the ParaView software.²⁴ Such structures representation were made to simplify the overall visualization, by transforming the set of discrete water molecules in continuous surfaces. To do so, a bounding surface around the water molecules has been calculated by mapping atom positions in a grid of $100 \times 100 \times 100$ cells. Each cell was filled by values of a spherical Gaussian distribution, adjusted from the radial distribution function (RDF), Fig S8A,B. For each water atom positions, the corresponding cell was filled by an arbitrary maximum value, while neighboring cells were filled following the spherical Gaussian distribution Fig S8C. The contribution of each atom was then summed to map all water atoms on rectilinear grid-cells. To extract the surface encompassing water molecules, the Gaussian distribution was adjusted with a radius of 0.3 nm, a threshold slightly larger than maximum averaged $O - H$ distances. We then extract cells whose field corresponds to a distance of 0.25 nm, corresponding to the full first $O - H$ intermolecular distances in the RDF, Fig S8B,D. The resulting representation of a continuous water network is shown in the Fig S8E.

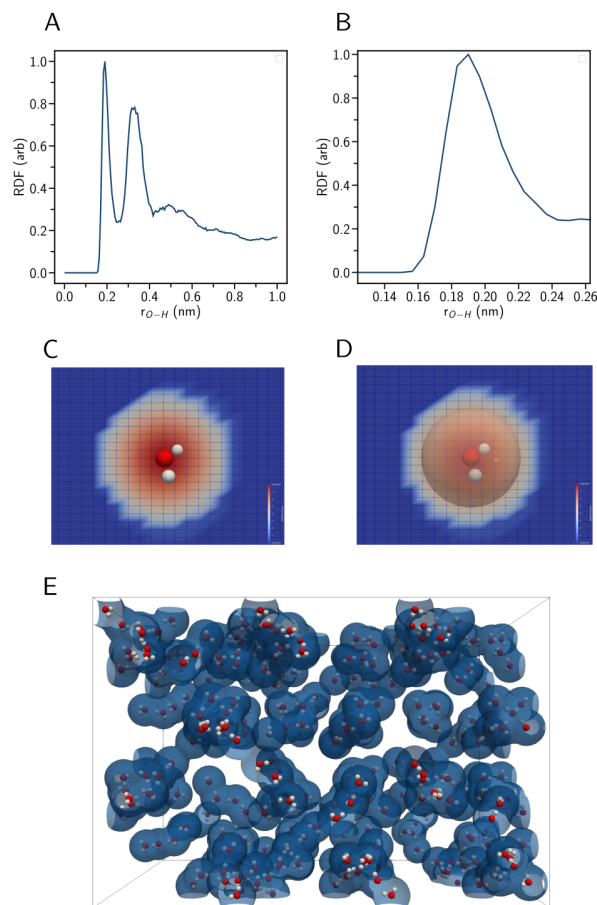


Figure S8: A. Water radial distribution function based on inter-molecular water hydrogen bonds $O - H$. B. Zoom of the first pic from the radial distribution function in (A). C. Mapping of one water molecule on a rectilinear grid-cells with a 3D Gaussian distribution. D. Extraction of a 3D contour around one water molecule corresponding to values of the field at a distance of 0.25 nm around the oxygen atom. E. 3D contour and continuum network representation of water medium.

References

- (1) Cavka, J. H.; Jakobsen, S.; Olsbye, U.; Guillou, N.; Lamberti, C.; Bordiga, S.; Lillerud, K. P. A new zirconium inorganic building brick forming metal organic frameworks with exceptional stability. *Journal of the American Chemical Society* **2008**, *130*, 13850–13851.
- (2) Valenzano, L.; Civalleri, B.; Chavan, S.; Bordiga, S.; Nilsen, M. H.; Jakobsen, S.; Lillerud, K. P.; Lamberti, C. Disclosing the complex structure of UiO-66 metal organic

- framework: a synergic combination of experiment and theory. *Chemistry of Materials* **2011**, *23*, 1700–1718.
- (3) Wu, H.; Chua, Y. S.; Krungleviciute, V.; Tyagi, M.; Chen, P.; Yildirim, T.; Zhou, W. Unusual and highly tunable missing-linker defects in zirconium metal–organic framework UiO-66 and their important effects on gas adsorption. *Journal of the American Chemical Society* **2013**, *135*, 10525–10532.
- (4) Ghosh, P.; Colón, Y. J.; Snurr, R. Q. Water adsorption in UiO-66: the importance of defects. *Chemical Communications* **2014**, *50*, 11329–11331.
- (5) Rouquerol, J.; Avnir, D.; Fairbridge, C.; Everett, D.; Haynes, J.; Pernicone, N.; Ramsay, J.; Sing, K.; Unger, K. Recommendations for the characterization of porous solids (Technical Report). *Pure and Applied Chemistry* **1994**, *66*, 1739–1758.
- (6) Park, J.; Howe, J. D.; Sholl, D. S. How reproducible are isotherm measurements in metal–organic frameworks? *Chemistry of Materials* **2017**, *29*, 10487–10495.
- (7) Wu, H.; Yildirim, T.; Zhou, W. Exceptional mechanical stability of highly porous zirconium metal-organic framework UiO-66 and its important implications. *The journal of physical chemistry letters* **2013**, *4*, 925–930.
- (8) DeCoste, J. B.; Peterson, G. W.; Jasuja, H.; Glover, T. G.; Huang, Y.-g.; Walton, K. S. Stability and degradation mechanisms of metal–organic frameworks containing the Zr₆O₄(OH)₄ secondary building unit. *Journal of Materials Chemistry A* **2013**, *1*, 5642–5650.
- (9) Winarta, J.; Shan, B.; McIntyre, S. M.; Ye, L.; Wang, C.; Liu, J.; Mu, B. A decade of UiO-66 research: a historic review of dynamic structure, synthesis mechanisms, and characterization techniques of an archetypal metal–organic framework. *Crystal Growth & Design* **2019**, *20*, 1347–1362.

- (10) Kökçam-Demir, Ü.; Goldman, A.; Esrafilı, L.; Gharib, M.; Morsali, A.; Weingart, O.; Janiak, C. Coordinatively unsaturated metal sites (open metal sites) in metal–organic frameworks: design and applications. *Chemical Society Reviews* **2020**, *49*, 2751–2798.
- (11) Kang, I. J.; Khan, N. A.; Haque, E.; Jhung, S. H. Chemical and thermal stability of isotopic metal–organic frameworks: effect of metal ions. *Chemistry–A European Journal* **2011**, *17*, 6437–6442.
- (12) Jiao, Y.; Morelock, C. R.; Burtch, N. C.; Mounfield III, W. P.; Hungerford, J. T.; Walton, K. S. Tuning the kinetic water stability and adsorption interactions of Mg-MOF-74 by partial substitution with Co or Ni. *Industrial & Engineering Chemistry Research* **2015**, *54*, 12408–12414.
- (13) Chanut, N.; Ghoufi, A.; Coulet, M.-V.; Bourrelly, S.; Kuchta, B.; Maurin, G.; Llewellyn, P. L. Tailoring the separation properties of flexible metal-organic frameworks using mechanical pressure. *Nature communications* **2020**, *11*, 1–7.
- (14) Mondloch, J. E.; Katz, M. J.; Planas, N.; Semrouni, D.; Gagliardi, L.; Hupp, J. T.; Farha, O. K. Are Zr 6-based MOFs water stable? Linker hydrolysis vs. capillary-force-driven channel collapse. *Chemical communications* **2014**, *50*, 8944–8946.
- (15) Peng, D.-Y.; Robinson, D. B. A new two-constant equation of state. *Industrial & Engineering Chemistry Fundamentals* **1976**, *15*, 59–64.
- (16) Manz, T. A.; Sholl, D. S. Chemically meaningful atomic charges that reproduce the electrostatic potential in periodic and nonperiodic materials. *Journal of Chemical Theory and Computation* **2010**, *6*, 2455–2468.
- (17) Campañá, C.; Mussard, B.; Woo, T. K. Electrostatic potential derived atomic charges for periodic systems using a modified error functional. *Journal of Chemical Theory and Computation* **2009**, *5*, 2866–2878.

- (18) Rappe, A. K.; Goddard III, W. A. Charge equilibration for molecular dynamics simulations. *The Journal of Physical Chemistry* **1991**, *95*, 3358–3363.
- (19) Wang, S.; Zhou, G.; Sun, Y.; Huang, L. A computational study of water in UiO-66 Zr-MOFs: Diffusion, hydrogen bonding network, and confinement effect. *AIChE Journal* **2021**, *67*, e17035.
- (20) Hossain, M. I.; Cunningham, J. D.; Becker, T. M.; Grabicka, B. E.; Walton, K. S.; Rabideau, B. D.; Glover, T. G. Impact of MOF defects on the binary adsorption of CO₂ and water in UiO-66. *Chemical Engineering Science* **2019**, *203*, 346–357.
- (21) Jajko, G.; Kozyra, P.; Gutiérrez-Sevillano, J. J.; Makowski, W.; Calero, S. Carbon Dioxide Capture Enhanced by Pre-Adsorption of Water and Methanol in UiO-66. *Chemistry (Weinheim an der Bergstrasse, Germany)* **2021**, *27*, 14653–14659.
- (22) Rivest, R. L.; Vuillemin, J. On recognizing graph properties from adjacency matrices. *Theoretical Computer Science* **1976**, *3*, 371–384.
- (23) Ebrahimpour-komleh, H.; Lazemi, S. Computing connected components of graphs. *International Journal of Applied Mathematics Research* **2014**, *3*, 508.
- (24) Ahrens, J.; Geveci, B.; Law, C. Paraview: An end-user tool for large data visualization. *The visualization handbook* **2005**, 717.